Organization and Structure of Clouds and Precipitation on the Mid-Atlantic Coast of the United States. Part II: The Mesoscale and Microscale Structures of Some Frontal Rainbands

JOSEPH M. SIENKIEWICZ, JOHN D. LOCATELLI, PETER V. HOBBS AND BART GEERTS

Atmospheric Sciences Department, University of Washington, Seattle, Washington

(Manuscript received 22 June 1988, in final form 8 November 1988)

ABSTRACT

The mesoscale and microscale structures of the clouds and precipitation associated with a frontal system on the mid-Atlantic Coast of the United States are investigated using radar reflectivity and Doppler velocity data, surface mesonet, conventional surface, upper-air and microphysical data. The frontal structure showed similarities to a warm occlusion, with cold-air advection aloft preceding cold-air advection at lower levels.

Six rainbands were observed in association with the frontal system. All of these rainbands developed within the region of coverage of the NWS WSR-57 radar at Cape Hatteras, North Carolina. Two were upper-level features, associated with a prefrontal surge of cold air and the main push of cold dry air aloft. These rainbands were similar in structure to prefrontal surge and wide cold-frontal rainbands, respectively, observed on the Pacific Northwest Coast. The microphysical and small mesoscale structures of the wide cold-frontal rainband are examined. Three of the rainbands were convective and developed at different times parallel to and just east of the warm-water core of the Gulf Stream. Each of these rainbands, in turn, migrated to the east. Coincident with the dissipation of the wide cold-frontal rainband offshore, a convective rainband developed behind the leading edge of the cold, dry air aloft and a third rainband intensified over the Gulf Stream in advance of the cold, dry air at midlevels. Mechanisms for the development of the Gulf Stream rainbands and for the dissipation of the wide cold-frontal rainband are discussed.

1. Introduction

In the first paper in this series (Locatelli et al. 1989, hereafter referred to as Part I) we described the evolution of the large-scale frontal structure of a cyclone as it moved eastward across the United States from 4 to 7 March 1986. Although this cyclone did not undergo the classical occlusion process, its frontal structure over the eastern Carolinas resembled a warm-type occlusion.

In this paper, we examine in more detail the mesoscale and microscale structures of this same frontal system as it passed through the special observing network of the Genesis of Atlantic Lows Experiment (GALE) on the Carolina coastal plain and out over the warm waters of the Gulf Stream.

A brief overview of the synoptic situation is given in section 3. Radar observations are described in section 4. The structure and airflow associated with an upper-level cold front are presented in section 5. A discussion of the development of rainbands over the Gulf Stream and the dissipation of a wide cold-frontal rainband is presented in section 6. Summary and conclusions are given in sections 7 and 8, respectively.

Corresponding author address: Dr. Peter V. Hobbs, Dept. of Atmospheric Sciences, AK-40, University of Washington, Seattle, WA 98195.

2. Location of field study and data sources

A detailed description of the observing systems used in GALE has been given in Part I. The location of the surface, sounding, and radar observing systems used in the present paper are shown in Fig. 1. The surface stations included National Weather Service (NWS) and military sites, NCAR Portable Automated Mesoscale (PAM-II) sites, and the Coastal-Marine Automated Network (C-MAN) sites. The PAM-II sites provided surface observations at 5 min intervals. One sounding site specific to this study consists of the NCAR Cross-chain Loran Atmospheric Sounding Systems (CLASS) site at Morehead City, North Carolina (MRH). In addition, soundings from dropwindsondes from the NOAA WP-3D aircraft are used.

The radar precipitation echo study, presented in section 4a, uses primarily data from the NWS 10.38 cm wavelength radar located at Cape Hatteras, North Carolina. This radar was equipped with a digital recorder for enhanced recording of radar precipitation echoes.

Vertical cross sections of radar precipitation echoes associated with a wide cold-frontal rainband were derived from the University of Washington's (UW) 35 GHz vertically pointing Doppler radar, which was located at Cape Hatteras. Streamline analysis and vertical air velocity data for this rainband were derived from

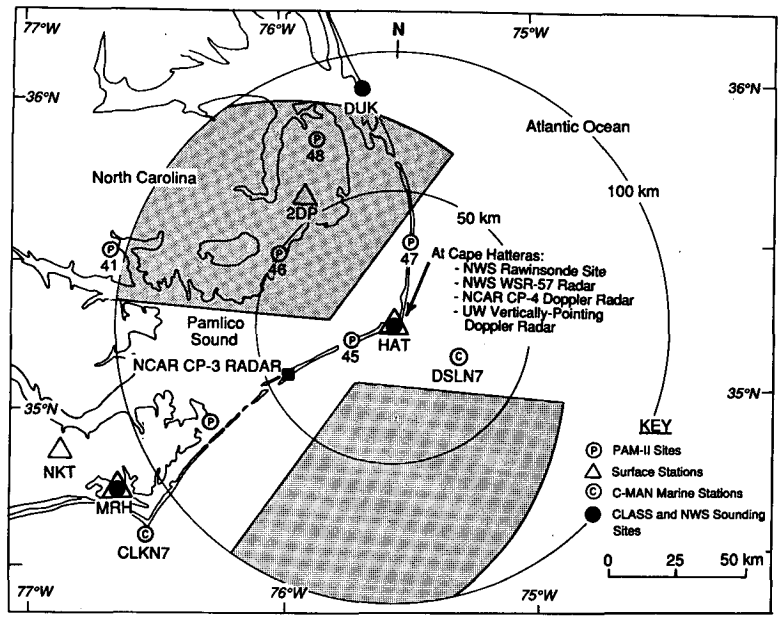

FIG. 1. GALE and NWS surface-based observational facilities, radiosonde sites and radar facilities used in this study. Range markers for 50 and 100 km indicate distance from the Cape Hatteras NWS WSR-57 radar. Shading indicates the extent of the dual-Doppler radar coverage from the NCAR CP-3 and CP-4 radars, which were located at Ocracoke Island and Cape Hatteras, respectively.

the NCAR 5.5 cm wavelength CP-4 and CP-3 Doppler radars, which were operated as a dual-Doppler pair. The CP-4 radar was located at Cape Hatteras and the CP-3 radar was situated ~40 km to the southwest of the CP-4 radar on Ocracoke Island (see Fig. 1). The two regions of dual-Doppler radar coverage, within which the recovery of detailed air velocity data was possible, are indicated by the shaded regions in Fig. 1.

In addition to the data sources listed here, cloud microphysical data were available from aircraft flights by the UW C-131A research aircraft. For a detailed description of the various instruments aboard this aircraft, the reader is referred to GALE (1985).

3. Synoptic situation

A detailed description of the evolution of the system to be described in this paper is given in Part I. Therefore, only a brief overview will be given here. The relevant surface data, frontal analysis, and precipitation echoes from six NWS radars for 1800 UTC 6 March are shown in Fig. 2. The surface front is situated ~225 km to the west of the two rainbands, labeled R1 and R2, which were associated with the leading edge of the cold-air advection aloft. Thus, the front bore similarities in structure to both a warm occluded front and a split cold front (Browning and Monk 1982), with cold-air advection aloft preceding cold-air advection at lower levels. The surface front and the locations of rainbands R1 and R2 and the rainbands over the Gulf Stream (GSR-1 and GSR-2), are indicated on the visible satellite imagery for 1731 UTC 6 March in Fig. 3. Clearly, the cloud mass associated with R1 and R2 was located well ahead of the surface front. Little or no cloud was associated with the surface front from the Virginia–North Carolina border southward.

Surface reports, shown in Fig. 2, show predominately southwesterly flow to the east and ahead of the surface front. The surface front at this time was not sharply defined in the temperature or wind fields. In this region, surface winds gradually veered and temperatures increased up to the front. The passage of the surface front was characterized by an additional veering of the surface wind and slight decreases in temperature and dewpoint. There was no surface wind shift associated with the passage of R1 and R2. Southerly surface flow is evident to the east of GSR-1 and GSR-2, with more southwesterly flow to the west of these rainbands.

4. The mesoscale structure and organization of the rainbands

a. Radar synopsis

In this section, we describe portions of the rainbands associated with the frontal system as observed by the NWS radar located at Cape Hatteras. The Volens, Virginia and the Cape Hatteras NWS radars first detected the development of precipitation at ~1200 UTC 6 March. The first indication of the development of an organized precipitation band to the northwest of Cape Hatteras within the range of the Cape Hatteras radar

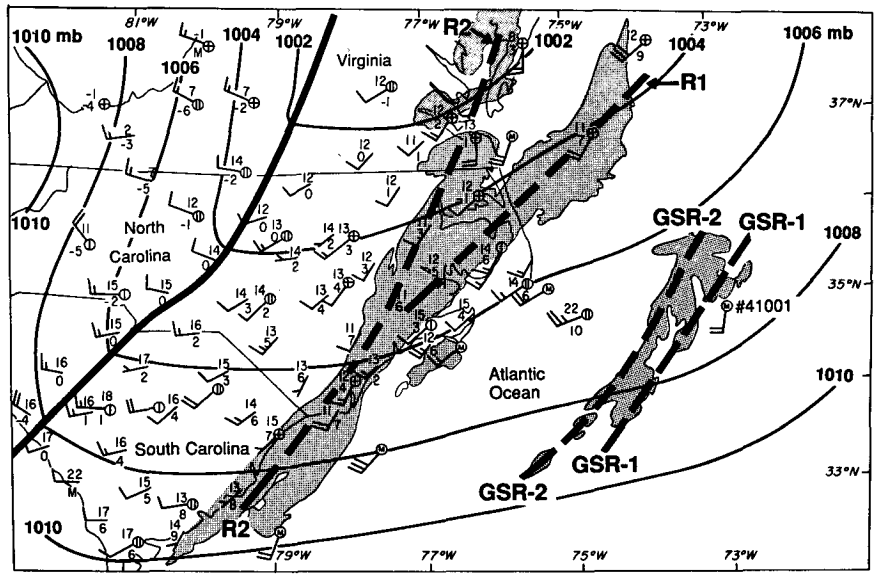

FIG. 2. Surface weather analysis for 1800 UTC 6 March 1986. Shown for each surface station is: temperature (°C) to the upper left of the station symbol, dewpoint temperature (°C) to the lower left of the station symbol, wind direction and speed, and skycover (in center of station symbol, for FAA and NWS sites only). Sky cover is shown using the following symbols: *open circle,* clear; *one vertical line,* scattered cloud; *two vertical lines,* broken cloud; *a cross,* overcast; and an *X*—sky obscured. Wind speeds are indicated by: *circle around station circle*—calm, *short barb*—2.5 m s^{-1}, *long barb*—5 m s^{-1}, and *flag*—25 m s^{-1}. The surface front is shown as a heavy solid black line. Rainbands R1 and R2 and the Gulf Stream rainbands (GSR-1 and GSR-2) are shown by the shading.

was at 1418 UTC 6 March; this is the rainband denoted as R1. By 1433 UTC another rainband had developed 150-170 km to the southeast of Cape Hatteras. This convective rainband was aligned in a northeast–southwest direction and parallel to the Gulf Stream. Following Hobbs (1987), we will refer to this as a Gulf Stream rainband (GSR-1).

The echo from the Cape Hatteras radar at 1458 UTC 6 March is shown in Fig. 4a. The axis of the warm-water core of the Gulf Stream is also shown in this figure. Rainband R1 is seen to be aligned in a northeast–southwest direction, ~160 km to the northwest of Cape Hatteras. The maximum radar reflectivities observed in R1 around this time were 24–36 dBZ. In addition to the main portion of R1, there is radar echo aligned in a more north–south direction (this substructure is labeled A in Fig. 4a). Three separate organized structures similar to A and associated with R1 were observed from 1343 to 1600 UTC.

The data from the NWS radar at Cape Hatteras indicates that GSR-1 was not advected into the region but developed in situ. The maximum radar reflectivity for GSR-1 was 24–36 dBZ. GSR-1 remained relatively stationary from 1458 to 1600 UTC, with precipitation cores moving to the northeast along the band. In addition, undulations were observed in the radar echo to propagate northward along the length of GSR-1 during this time period. After 1600 UTC, GSR-1 drifted slowly to the southeast. Between 1703 and 1729 UTC a second Gulf Stream rainband (GSR-2), aligned parallel and to the west of GSR-1, developed in approximately the same location as GSR-1. Rainband R2, first observed at ~1730 UTC, was similar in orientation to the small-scale precipitation band A previously discussed and shown in Fig. 4a.[1]

The precipitation echoes observed with the NWS radar at Cape Hatteras at 1813 UTC 6 March are shown in Fig. 4b. The two Gulf Stream rainbands (GSR-1 and GSR-2) can be seen to the southeast of the radar. The maximum radar reflectivity in GSR-2 was >36 dBZ. Rainband R1 extended from the north-northeast of Cape Hatteras to the point where it intersected with R2. Rainband R1 had a relatively narrow core of maximum reflectivity with values of 36–42 dBZ. Rainband R2 was located to the west of R1, and aligned in a more north–south direction. A minimum of radar reflectivity can be seen between R1 and R2.

By 2006 UTC, very little of R1 was evident to the northeast of Cape Hatteras (Fig. 4c). The leading edge of R2 was approaching Cape Hatteras. In a comparison of the 1813 and 2006 UTC radar displays, it is apparent that R1 and R2 were moving at a higher velocity than GSR-2; GSR-2 moved very little from 1813 to 2006

[1] A detailed description of the chemistry of rainband R2 will be described in a paper by Hegg et al. (*Quart. J. Roy. Meteor. Soc.,* in press).

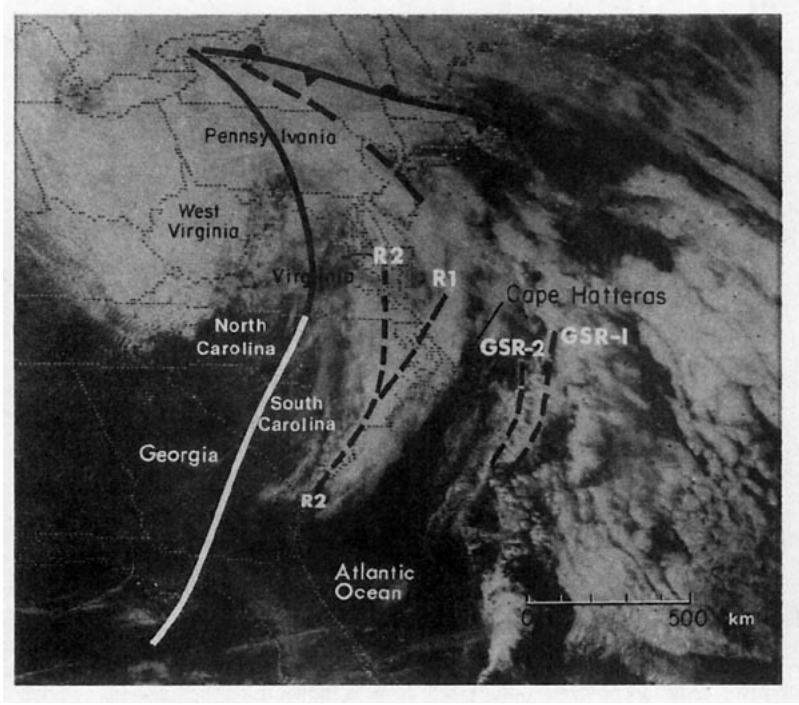

FIG. 3. Visible satellite image for 1731 UTC 6 March 1986. The locations of surface frontal features and rainbands R1, R2, and the Gulf Stream rainbands (GSR-1 and GSR-2) are shown. The surface front is shown by a solid black then white line; the pressure trough by a dashed line; and the stationary front by standard symbols.

UTC. At 2006 UTC, GSR-1 was no longer evident. However, due to range limitations of the Cape Hatteras radar, it is unclear whether GSR-1 dissipated as it moved off to the southeast.

Precipitation in the form of light rain began falling at Cape Hatteras at 2008 UTC and ended at 2033 UTC. The PAM-II surface observations showed that the maximum precipitation associated with R1 and R2 occurred at the junction of R1 and R2, in the region marked B in Fig. 4b.

A further series of radar displays from Cape Hatteras is shown in Fig. 5. The 2104 UTC (Fig. 5a) display shows rainband R2 to the east of Cape Hatteras. A relatively narrow core of maximum radar reflectivity (>36 dBZ) is present in R2. At 2104 UTC, the axis of GSR-2 is located at a minimum of 210 km from Cape Hatteras.

Prior to the dissipation of R2, a third Gulf Stream rainband (GSR-3) developed parallel to and to the west of GSR-2. Some convective cells to the west of GSR-2 can be seen at 2104 UTC (Fig. 5a). By 2149 UTC (Fig. 5c), rainband GSR-3 was fully developed. The maximum radar reflectivities observed during this study (>48 dBZ) were associated with GSR-3. It should be noted that all of the Gulf Stream rainbands observed on 6 March 1986 developed in the same location (150–170 km southeast of Cape Hatteras and ~20 km to the east of the warm-water core of the Gulf Stream).

In a comparison of the four displays shown in Fig. 5, the dissipation of R2 is evident. As R2 proceeded to the southeast of Cape Hatteras, a decrease in the areal extent of maximum reflectivity (>36 dBZ) can be seen. This is particularly evident from 2119 to 2149 UTC. By 2239 UTC (Fig. 5d), R2 had almost completely dissipated as it approached GSR-3. This dissipation was confirmed by aircraft observations.

A region of convection (evidenced by more cellular structure in the radar echoes and confirmed by aircraft observation) was present ~35 km to the west of the remnants of R2 at 2239 UTC (labeled as R3 in Fig. 5d). This rainband developed between 2200 and 2239 UTC 6 March, concurrent with the dissipation of R2. Rainband R3 continued to develop and move to the southeast, and by ~0100 UTC 7 March was beyond the range of the Cape Hatteras radar.

To summarize, six rainbands were observed by the NWS radar at Cape Hatteras on 6 March 1986. Three of these bands (GSR-1, GSR-2, and GSR-3) developed 150–170 km to the southeast of Cape Hatteras parallel to the warm-water core of the Gulf Stream. Rainband R1 developed to the west of Cape Hatteras at ~1418 UTC. Three smaller precipitation structures, oriented in a more northerly–southerly direction, were associated with R1. Rainband R2, which developed to the west of R1 was oriented in a similar manner to these three structures. Rainband R2 dissipated to the east of Cape Hatteras as it approached GSR-3. Coincident

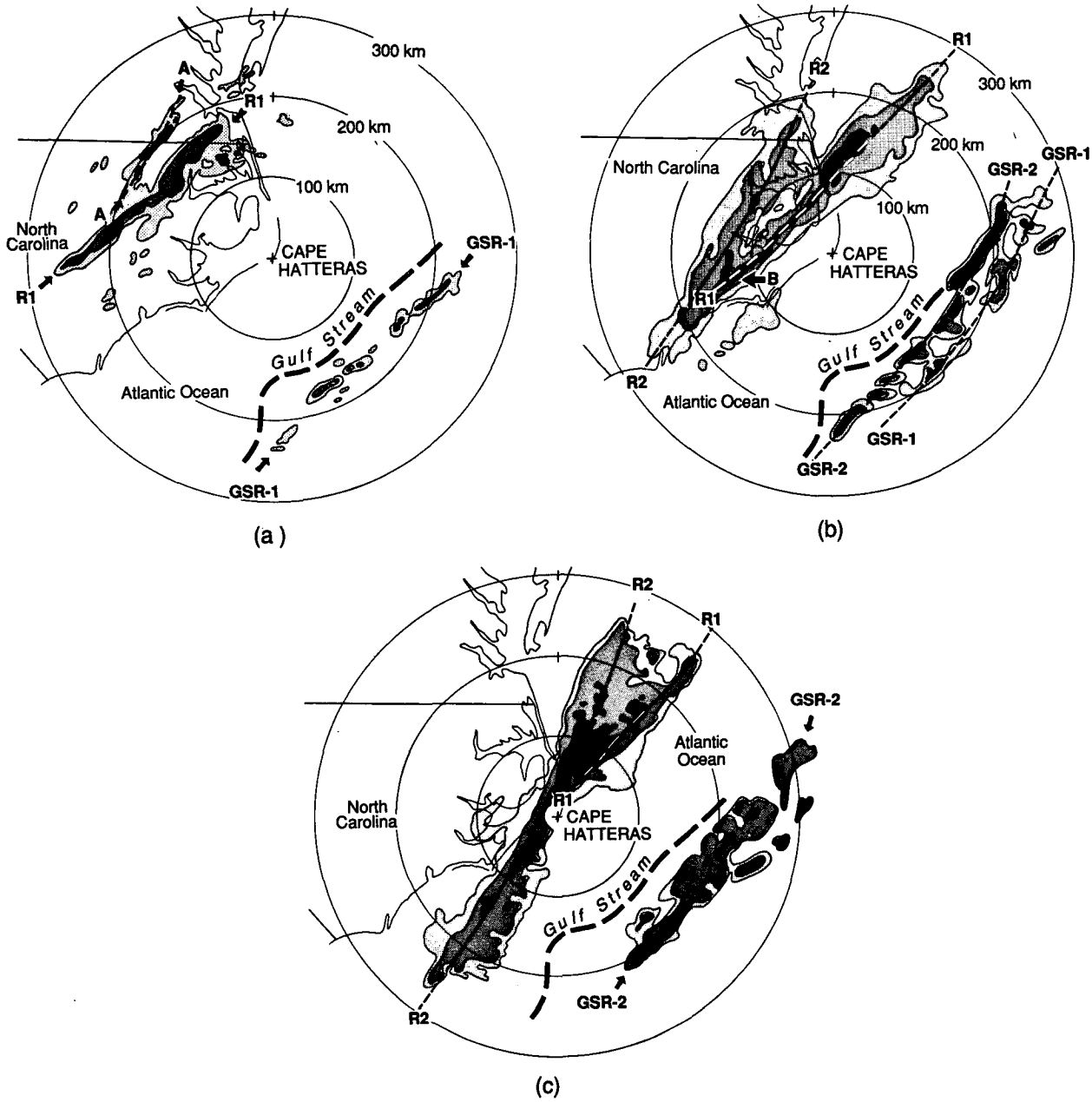

FIG. 4. Radar PPI scans from the Cape Hatteras, North Carolina, NWS 10.38 cm wavelength radar for (a) 1458 UTC, (b) 1813 UTC and (c) 2006 UTC 6 March 1986. Radar reflectivity contours are indicated by: light shading, 12-24 dBZ, medium shading, 24-36 dBZ, and dark shading, >36 dBZ. The small-scale precipitation feature to the west of R1 is labeled A in (a). The maximum precipitation in rainbands R1 and R2 was associated with region B in (b). The approximate location of the axis of the warmest water of the Gulf Stream is shown by a bold dashed line.

with the dissipation of R2 was the development of a more convective rainband (R3) located ~35 km to the west of R2.

b. Rainband motion and precipitation core motion

We now describe the motions of the six rainbands and regions of radar reflectivity maxima within the rainbands. Following Hobbs and Locatelli (1978), we will refer to small mesoscale areas of higher intensity precipitation embedded within larger areas of precipitation as *precipitation cores.*

The precipitation cores observed in this study averaged 50–500 km^2 in horizontal area. Shown in Table 1 are the mean motions (normal to their lengths) of the six rainbands described in section 4a, and the mean

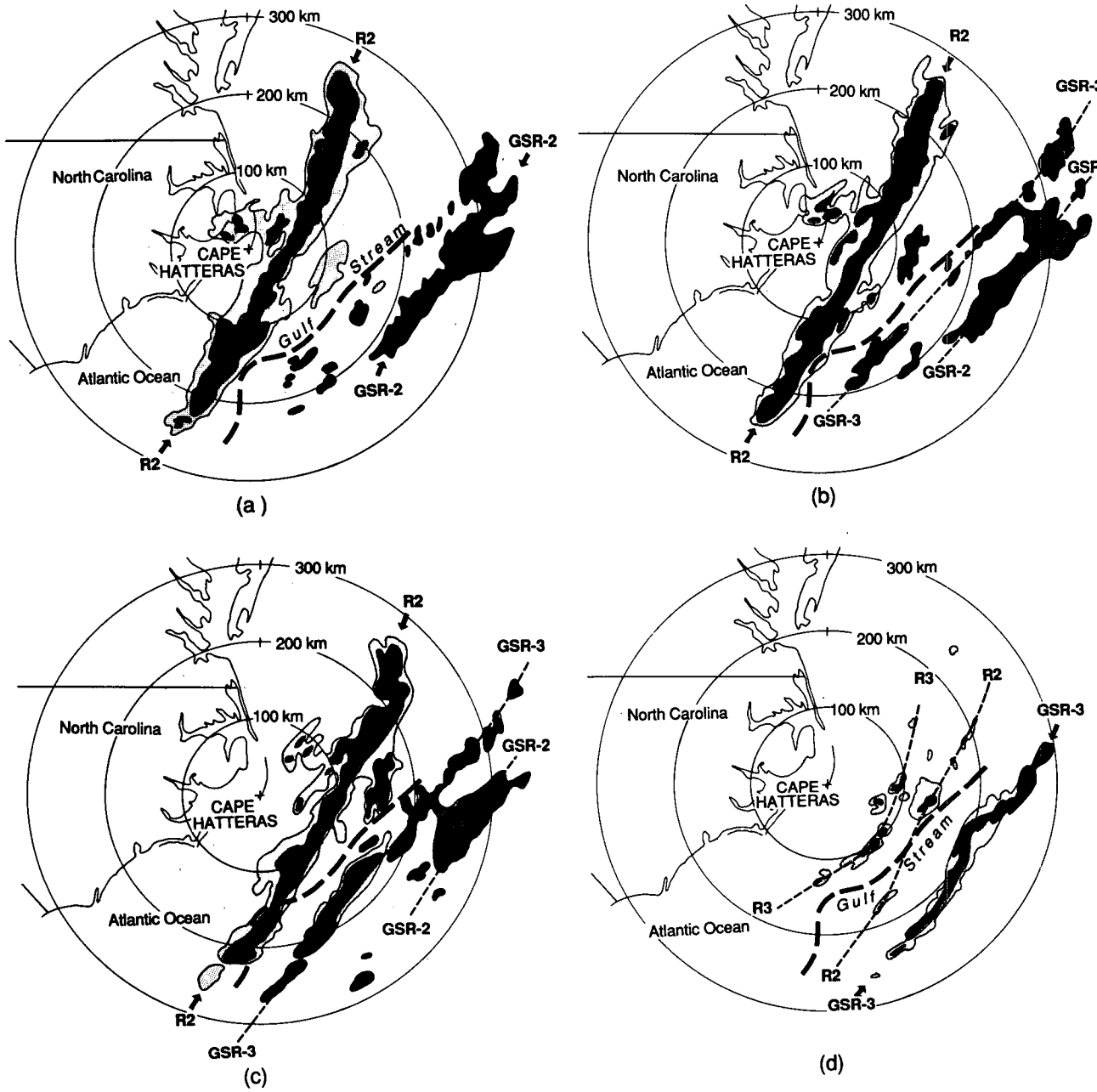

FIG. 5. As for Fig. 4, but for (a) 2104 UTC, (b) 2119 UTC, (c) 2149 UTC and (d) 2239 UTC 6 March 1986.

motions for the precipitation cores in these bands. These motions were obtained by tracing the movements of radar echoes every 15 min from 1233 UTC 6 March to 0059 UTC 7 March.

Although R1 and R2 had different mean motions, the motions of their cores were similar. Although the Gulf Stream rainbands, GSR-1 and GSR-2, were nearly stationary, precipitation cores within them had large speeds ($\sim$17 and 19 m s^{-1}, respectively) along the length of the bands. The cores in GSR-3 had a more easterly motion than those in GSR-1 or GSR-2. The increasingly easterly component of the core motion with time appeared to be associated with an increasing westerly low-level wind, as the upper-level trough moved off the Atlantic Coast. In each of the six rainbands, the component of core motion normal to the length of the rainband was approximately the same as the motion of the rainband.

The steering levels for the precipitation cores, determined by comparing rawindsonde data with the motions of the precipitation cores, are also listed in Table 1. The steering levels for the more stratiform

TABLE 1. Mean motions of the rainbands and precipitation cores observed on 6 March 1986.

	Rainband		Precipitation Cores			
Rainband	Moved toward (deg true)	Velocity ($m\ s^{-1}$)	Number of qualifying cores	Moved toward (deg true)	Velocity ($m\ s^{-1}$)	Steering level (km)
R1	134	8.6	34	64	25	3.2–4.4
R2	123	15.9	27	63	27	3.2–4.4
R3	129	17.2	11	74	25	
GSR-1	*	*	14	47	17	
GSR-2	128	6.3	26	47	20	
GSR-3	128	11.7	13	54	27	

* Rainband GSR-1 was stationary from 1400–1600 UTC 6 March.

rainbands R1 and R2 were 3.2–4.4 km in altitude. Because of the scarcity of upper-level wind data offshore, steering levels are not listed for GSR-1, GSR-2, GSR-3 and R3.

c. *Precipitation amounts*

The precipitation amounts associated with R1 and R2 along the mid-Atlantic Coast are shown in Fig. 6. The maximum precipitation, which was located at the intersection of R1 and R2 (B in Fig. 4b), was recorded at stations west of Pamlico Sound in eastern North Carolina.

5. The small mesoscale structure of rainband R2

In this section we examine the kinematic, thermodynamic and cloud microphysical aspects of rainband R2 using data from the UW vertically pointing 35 GHz radar, the dual-Doppler radars, and the UW C-131A research aircraft.

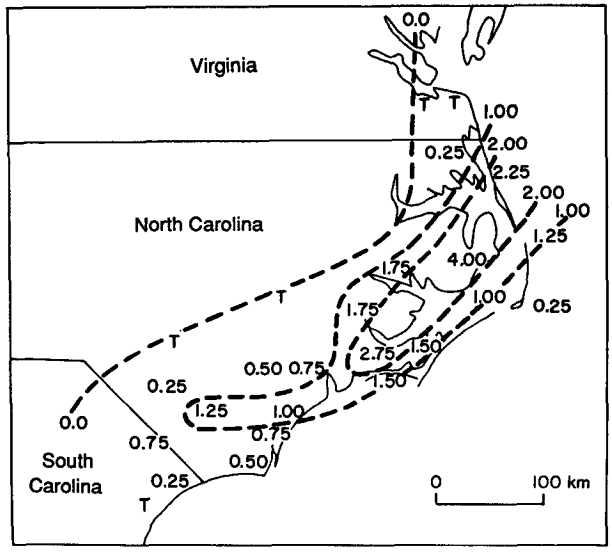

FIG. 6. Map of eastern North Carolina showing total accumulated precipitation amounts in millimeters from rainbands R1 and R2. Contours (dashed lines) are for precipitation amounts of 0.0 mm, 1.00 mm, and 2.00 mm. A trace of precipitation is indicated by a T.

a. *Vertical structure of precipitation*

A vertical cross section of the precipitation echoes associated with R2, as detected by the 35 GHz vertically pointing radar located at Cape Hatteras, is shown in Fig. 7. In Fig. 7 time has been converted to distance assuming that the echo was moving at the speed of rainband R2. This cross section is for the portion of R2 located south of its intersection with R1. Two fallstreaks (A and B in Fig. 7) were located at the leading edge of this rainband. Precipitation from these fallstreaks did not extend to the surface. Protrusions at the base of the leading edge of R2 (E in Fig. 7) indicate a region of evaporation. The precipitation from the fallstreak C in Fig. 7 did reach the surface.

Hobbs et al. (1985) noted that the 35 GHz radar echo generally exhibits a peak in reflectivity just below the base of the melting layer. The top of this region of maximum reflectivity is labeled D–D′ in Fig. 7. The relatively sharp upper boundary of the reflectivity maximum indicates that precipitation in this region was stratiform in nature. Cumuliform precipitation is evident at lower levels to the rear of R2; the melting layer is not as clearly defined in this region as in the stratiform region. Immediately above the low-level cumulus there was no radar echo. The evaporation of precipitation falling into this dry slot is indicated by the protrusions (F in Fig. 7). The details in precipitation echo seen at the leading edge of R2 are not evident above the main precipitation region. This is most likely due to attenuation of the radar signal.

A change in structure can be seen across the width of R2. The leading edge of R2 contains fallstreaks at midlevels but no cloud or precipitation below 1.5 km. The main precipitation region was ~25 km in width and stratiform in nature. A break in the precipitation reaching the ground and a change in character to more cumuliform precipitation occurs at ~ −20 to −23 km in Fig. 7 along the x-axis.

The surface data from PAM-II station 45 (see Fig. 1) is shown at the base of Fig. 7. There was little or no change in wind speed or direction with the passage of R2 at this station. The temperature decreased 1.5°C with the onset of rain at this station and was most

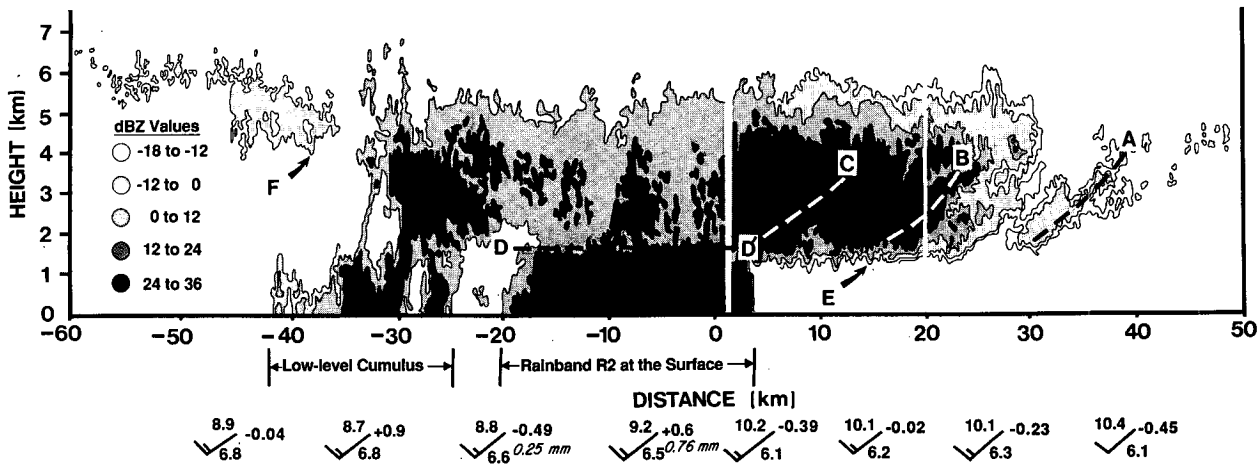

FIG. 7. Vertical cross section of radar reflectivity for rainband R2 from the 35 GHz radar. The darker the shading, the stronger the echo strength. The 15 min surface reports from PAM-II station 45 (see Fig. 1) are shown. Surface data is plotted as in Fig. 2 with the following additions: pressure tendency is shown to the right of the station model (±mb) and accumulated precipitation (mm) is shown to the lower right of the station model.

likely due to evaporation. In addition, the dewpoint temperature increased 0.7°C with the passage of R2. The net effect is that the equivalent potential temperature barely changed (−0.6°C). There was a drop in surface pressure ahead of R2, and a slight rise in pressure with the onset of rain at the surface. A second rise in pressure occurred as the cumulus clouds to the rear of R2 passed over the station. Precipitation was associated with the main portion of R2, but there was no precipitation recorded at the surface associated with the cumulus in the rear portion of R2.

b. *Relative airflow and θ_e structure*

The equivalent potential temperature (θ_e) field across R2 is shown in Fig. 8a. The 1800 and 2100 UTC soundings from Morehead City (MRH in Fig. 1) and aircraft flight level data were used to derive the θ_e field shown in Fig. 8a. The sharp increase in θ_e with height shows that there was a stable layer at the base of the leading edge of R2. The isentropes associated with this stable layer slope gradually toward the surface across the width of R2. This stable layer corresponds to the zone of warm-air advection shown in cross sections E–E′ and F–F′ in Fig. 12 of Part I. It is analogous to the zone of warm-air advection associated with the warm front in a warm occlusion.

A wedge of low θ_e air was present to the rear of R2 (Fig. 8a). The double line is drawn along the 306 K isentrope to indicate the boundary between air with low θ_e and high θ_e values. Thus, this line marks the leading edge of the cold-air advection aloft; it corresponds to the leading edge of the cold-air advection shown in Fig. 14 of Part I. This is analogous to the upper-level cold front in a warm occlusion.

A zone of maximum θ_e extends from the base of the leading edge of cold-air advection aloft to the surface front. This zone is similar to the upper portion of the occluded front in a warm occlusion. There is a layer of potentially unstable air below the region of minimum θ_e in the rear portion of R2. This is the region of low-level cumulus.

Streamlines of the mean airflow relative to the motion of R2, and the mean vertical velocity field derived from the dual-Doppler velocity data, are shown in Fig. 8b. The radial velocities and reflectivities from the CP-3 and CP-4 radars were interpolated to a storm-relative Cartesian grid of 1.5 × 1.5 × 0.6 km spacing. Vertical air velocities were derived from the anelastic continuity equation subjected to a double boundary condition; the horizontal flow was not readjusted to allow for the second boundary condition. The streamline analysis indicates that the main region of convergence was situated ahead of the leading edge of cold-air advection at a height of ~2–6 km. Below 2 km, front-to-rear airflow can be seen with descending flow below and ahead of the nose of cooler drier air. Upward vertical motions are present from ~25 km to −5 km along the horizontal axis and above a height of 2 km. Two large regions of maximum vertical velocity can be seen in advance of the leading edge of cooler drier air, one located at ~20 km on the horizontal axis with a maximum value of 1.5 m s^{-1}, and the other is above the nose of cool dry air and extending from 2.5 to 6 km in height. (The circulation above the upper-level front, from −10 to −20 km on the horizontal axis, is sensitive to slight changes in the speed of the rainband and may be an artifact.)

c. *Microphysical structure*

The types and maximum sizes of the cloud and precipitation particles encountered along various flight tracks through R2 are shown in Fig. 9a. Dendritic ice

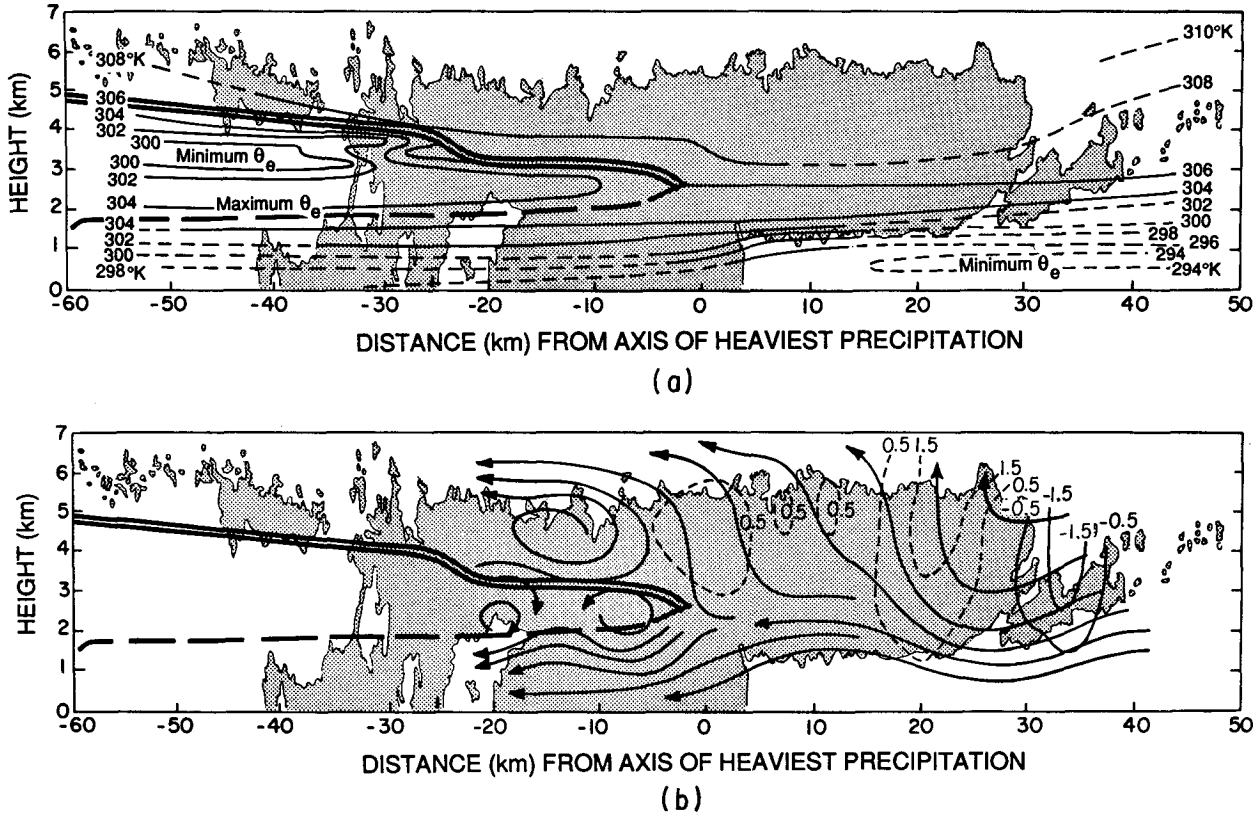

FIG. 8. Vertical cross sections through rainband R2 of (a) equivalent potential temperature (θ_e) from aircraft and sounding data, and (b) streamlines (solid lines) and vertical velocity (dashed contours, labeled in m s^{-1}) derived from dual-Doppler radar data. The shaded region shows the outline of radar reflectivity from the UW 35 GHz vertically pointing radar. The leading edge of the cold dry air aloft is indicated by a double bold line. A maximum of θ_e extending from the base of the leading edge of cold, dry air aloft is shown by the bold dashed line.

crystals were the dominant particles observed ahead of the push of cold, low θ_e air, although a few needles and sheaths were also present. It can be seen from Figs. 8 and 9a that the growth layer for needles and sheaths was located at the base and in the weakest portion of the updraft. Thus, the sparsity of needles and sheaths is due to the position of the main updrafts relative to the height of the diffusional growth layer for these types of ice crystals. The dendritic growth layer, on the other hand, was located within the strongest portion of the updraft.

Some dendrites were also observed behind the nose of cold dry air. However, the majority of precipitation particles above 2.5 km were unidentifiable. Below 2.5 km, in this region, a variety of particle types were observed, including graupel, dendrites, cloud droplets and unidentifiable crystals. The graupel and cloud droplets reflect the convective nature of the region behind the surface rainband, in the region of decreasing θ_e with height that is situated directly above the maximum in θ_e.

The largest particles were found ahead of the push of cold, dry air. These were aggregates of dendrites up to 15 mm in diameter. Behind the push of cold, dry air, the particles were smaller, up to 6 mm in diameter. The largest particles observed were associated with the precipitation that formed in the main updrafts of the rainband. These particles fell to the rear of the main updrafts in R2. The region near 2 km in height, where 14 mm diameter aggregates were observed, was just above the melting level, directly over the heaviest precipitation. A precipitation rate of 3.72 mm h^{-1} was calculated from the aircraft precipitation particle data in this region; this agrees fairly well with the precipitation rate of 4.40 mm h^{-1} observed below this location on the ground. Even though the particles ranged from <1 mm to >15 mm in diameter, more than 48% of the precipitation was due to particles from 2 to 6 mm in diameter.

The liquid water content across rainband R2 is shown in Fig. 9b. Maximum values (<1.0 g m^{-3}) are located in the convective region behind the surface rainband. In contrast, only two small regions of liquid water were found ahead of the push of cold, dry air. The existence of graupel in the convective region indicates heavy riming. Unrimed dendrites were encountered at ~3.5 km in height ahead of the push of cold dry air.

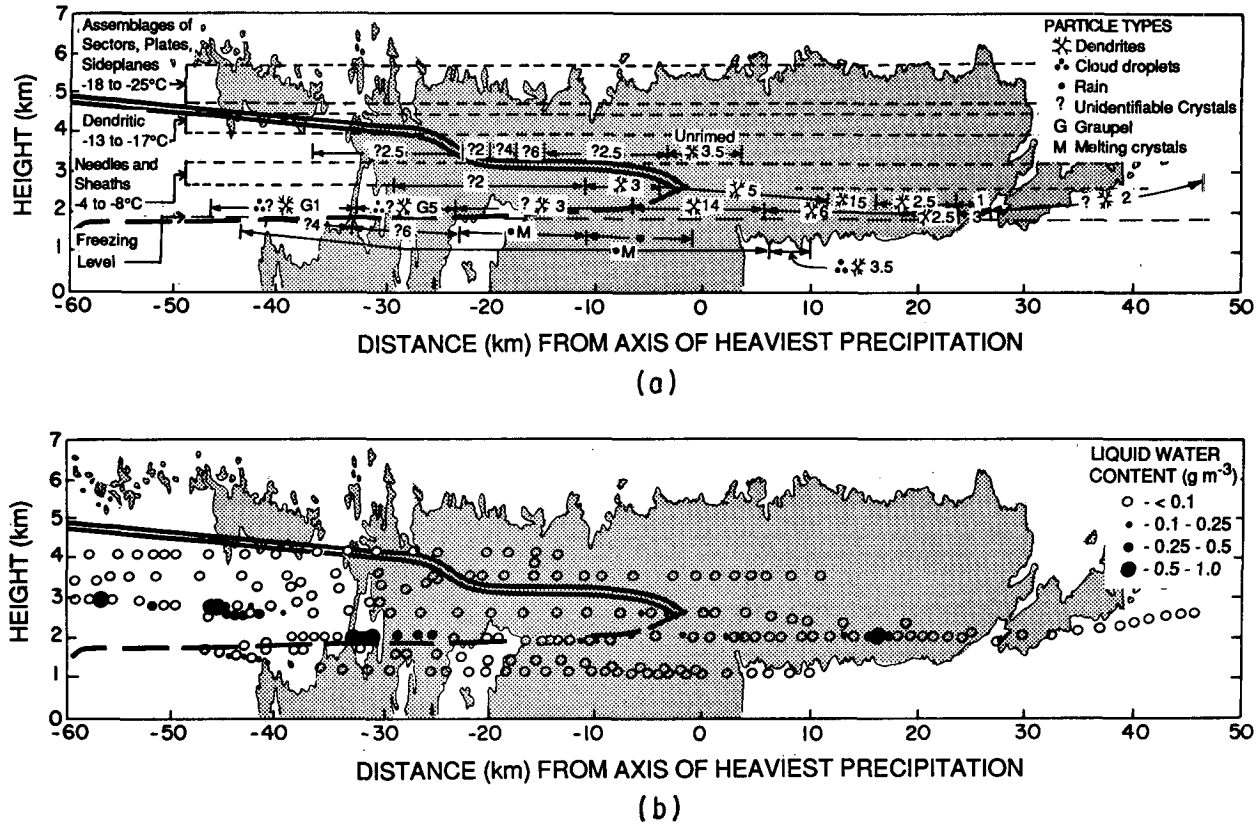

FIG. 9. Vertical cross sections through rainband R2 of (a) particle type, maximum diameter of particles (mm), diffusional growth regions for various particle types (narrow dashed lines), and freezing level, and (b) liquid water content (in g m^{-3}). Symbols used to indicate upper-level features are as in Fig. 8.

6. Discussion

a. Classification of the rainbands

A classification of the mesoscale rainbands observed in cyclones on the Pacific Northwest Coast has been described by Hobbs (1978). In this section, we compare the rainbands described in this paper with those discussed by Hobbs.

As we have seen, rainbands R1 and R2 were associated with a frontal structure similar to a warm occlusion, in that cold-air advection aloft preceded cold advection at lower levels and the surface front by ~225 km. However, this frontal structure was observed in a portion of the cyclone that did not undergo the classical occlusion process (see Part I). Rainbands associated with the upper-level cold front in the occluded portion of a cyclone were termed wide-cold frontal rainbands by Hobbs (1978). As described in section 5 of this paper, R2 was situated at the leading edge of cold-air advection aloft associated with an upper-level cold front. Therefore, R2 can be classified as a wide cold-frontal rainband.

In Part I we associated rainband R1 with a surge of cold air ahead of the primary cold front aloft. Although the orientation of R1 was in a more northeast–southwest direction than R2, it can be seen from Table 1 that the motion of the precipitation cores in R1 and R2 were similar. This suggests that the precipitation from R1 originated from the same height as R2. In the classification scheme of Hobbs (1978), R1 would be termed a prefrontal surge rainband.

Rainband R3 was convective, situated behind the leading edge of cold air aloft, and oriented parallel to both the upper-level and surface fronts (see section 4). It was suggested by Kreitzberg and Brown (1970) that the release of potential instability behind a prefrontal surge could result in the development of thunderstorms or squall lines. However, unlike the case described by Kreitzberg and Brown, R3 developed in a region of potentially unstable air behind the main push of cold air aloft or upper-level cold front, not behind a prefrontal surge.

Similarities between the frontal structure described in this paper and the split cold-front model of Browning and Monk (1982) were discussed in Part I. Browning and Monk suggested that the region of potential instability behind the upper-level cold front may often contain weak convective elements and sometimes regions of deep convection. The aircraft observations and the vertically pointing radar data described in this paper

indicate that as R2 moved over the Outer Banks of North Carolina, weak convection was present behind the leading edge of cold advection aloft. Rainband R3 developed as this region of weak convection reached the relatively warm inshore waters off the Carolina coast. Therefore, a transition occurred from weak convection to deep convection behind the leading edge of cold air aloft. Since the steering level for the precipitation cores in R3 was within the planetary boundary layer (PBL), R3 (unlike R1 and R2) probably originated in the PBL.

As described by Hobbs (1978), convective rainbands on the West Coast are observed in the warm sector of cyclones (warm-sector rainbands), on the surface cold front (narrow cold-frontal rainbands), and within the unstable air behind the cold front (postfrontal rainbands). However, R3 does not fit any of these types of convective bands.

The Gulf Stream rainbands described in this paper, which developed in the warm-sector of the cyclone in advance of the upper-level push of cold dry air aloft, were first identified by Hobbs (1987); these rainbands have no equivalent on the West Coast. They are discussed further here.

b. *The Gulf Stream rainbands*

Distinct weather changes have been observed off the Carolina coast along the boundary between the Gulf Stream and the inshore shelf water. Sweet et al. (1981) pointed out that fog and haze may persist over the cooler inshore shelf water while better visibility and convection may exist over the Gulf Stream. Fett et al. (1979), in a study using visible satellite imagery, observed a persistent cloud band located northeast of Florida over the eastern boundary of the Gulf Stream. Hobbs (1987) noted that the Gulf Stream rainband (GSR-2) observed in the case described in this paper developed on the eastern edge of the warm waters of the Gulf Stream. The cloud bands observed by Fett were also situated to the east of the warmest waters of the Gulf Stream. Hobbs suggested that unstable conditions, and the development of convective rainbands over the Gulf Stream are due to the large fluxes of heat and moisture in this region. Hobbs also suggested that the observed displacement of these rainbands in southwesterly winds to the east of the core of warmest waters of the Gulf Stream was due to the time required for precipitation particles to grow to a size detectable by radar. In addition, it was suggested by Hobbs that the Gulf Stream may act as a heat island and the Gulf Stream rainband may be part of a thermally induced direct circulation.

The more detailed radar analysis presented in this paper reveal that the Gulf Stream rainband observed on 6 March 1986 actually consisted of three separate rainbands (see section 4). Each of these rainbands developed in approximately the same location in relation to the Gulf Stream (~20 km to the southeast of the center of the warm-water core of the Gulf Stream). Although GSR-1 was nearly stationary for 2 h, it eventually drifted off slowly to the southeast. The subsequent Gulf Stream rainbands (GSR-2 and GSR-3) had progressively greater velocities to the southeast. Also, as documented in section 4, the motions of the precipitation cores in these rainbands was increasingly eastward with the passage of time. This is attributed to the increasing westerly component of the winds at the steering level (the PBL) for these rainbands.

The first precipitation echoes associated with GSR-1 were observed ~5 h after the onset of a southwesterly surface wind at NOAA buoy 41001 (located ~25 km to the east of GSR-1 and GSR-2 in Fig. 2). After 1400 UTC the wind at buoy 41001 backed slightly to become near southerly, and by 1600 UTC it had increased in strength from 7.5 to 12.5 m s^{-1}. The 1800 UTC surface map shown in Fig. 2 indicates a relatively sharp trough just to the west of buoy 41001 and GSR-1 and GSR-2. Southerly flow at buoy 41001 suggests that at the lowest levels there was inflow of air (i.e., SE to NW relative to GSR-1 and GSR-2) and low-level convergence associated with GSR-1 and GSR-2. We suggest that in the presence of low-level flow (southwesterly, in this case) parallel to the Gulf Stream, air parcels receive considerable heating due to their long trajectories over the Gulf Stream and this is conducive to the development of convective rainbands over the Gulf Stream off the Carolina coast.

The movement of the Gulf Stream rainbands eastward, away from the warm-water core of the Gulf Stream, was probably due to the increasing westerly component of the lower-level wind. When the eastward moving rainband had moved a sufficient distance to the east of the Gulf Stream core, so that its related downdraft had also moved east of this region, a new Gulf Stream rainband developed. This can be seen in Fig. 5. Thus, GSR-3 developed when GSR-2 was ~50–60 km to the east of the core of the Gulf Stream.

A climatological study of Gulf Stream rainbands is needed to understand better the large-scale conditions needed for their development. Also, the effects on cyclogenesis of convection, as well as associated latent heat release, over the Gulf Stream need to be examined. As discussed in Part I, a significant low-pressure system developed along the northern edge of the Gulf Stream between 0000 and 0600 UTC 7 March 1986, which was about 12 h after the appearance of the Gulf Stream rainbands described in this paper.

c. *Precipitation processes in rainband R2*

Cyclonic storms on the U.S. West Coast often contain small-scale convective elements aloft called generating cells, which can play an important role in the formation of precipitation (Hobbs and Locatelli 1978). Generating cells are regions of relatively higher vertical air velocity, occasional liquid water, and high ice crystal concentrations. Ice particles from the generating cells may grow by deposition, aggregation and riming as

they fall through lower cloud layers (the "seeder-feeder" mechanism—Hobbs 1978). In this way, generating cells can increase precipitation over small mesoscale areas on the ground. Hobbs et al. (1980) and Herzegh and Hobbs (1980) deduced from case studies that about 20% of the mass of precipitation reaching the ground in a rainband dominated by the seeder-feeder process originates in the seeder zone and about 80% is collected by the "seed" crystals as they fall through the feeder zone.

There is circumstantial evidence that a seeder–feeder process operated in the rainband R2 described in this paper. Fallstreaks of heavier precipitation were embedded in the more uniform precipitation ahead of the surface rainband (see section 4 and Fig. 7). Aggregates of dendrites in concentrations of $\sim 5\ L^{-1}$ were observed from the aircraft in these regions. Since each aggregate was comprised of several ice crystals, the concentration of crystals in this (feeder) region was much greater than would be expected from natural ice nuclei. High ice particle concentrations such as this have been linked to crystals falling from seeder zones aloft (Locatelli et al. 1983). Unfortunately, neither the aircraft nor radar data extended into the upper regions of R2 where the seeder zone would have been located.

Matejka et al. (1980) described a rainband over the Pacific Coast on 7 January 1975 that was similar to R2. The rainband described by Matejka et al. was also associated with an upper-level cold front in a warm-type occlusion; and it was stronger than R2 in that it had mean and maximum updrafts of 2 and 6 m s^{-1}, respectively, compared to 0.6 and 1.8 m s^{-1} in R2. The maximum liquid water content in the updraft zone of the Pacific Coast rainband was ~ 0.5 g m^{-3}, and there was liquid water across the whole updraft region. Similar values of liquid water were found in R2, but only in spotty regions. Graupel and heavily rimed aggregates were found in the Pacific Coast rainband and unrimed to lightly rimed aggregates in R2. Maximum precipitation in the Pacific Coast rainband, was 23 mm h^{-1}, compared to 4.4 mm h^{-1} in R2. A rise in the surface pressure and veering of the surface wind occurred as the cold front passed aloft on the Pacific Coast. In R2 the pressure rose slightly as the cold air aloft passed over but the surface wind did not shift (Fig. 7).

Thus, even though the strength of R2 was less than that of the Pacific Coast rainband described by Matejka et al. their overall structures were similar. In both cases convection occurred behind the upper-level push of cold, dry air and above the zone of maximum θ_e. Also, in both cases clearing occurred at midlevels behind the main region of cold-frontal cloud, with some virga falling from the upper-level cloud deck into the clear region below.

d. Dissipation of rainband R2

During the GALE study of 6 March 1986 it was anticipated that R2 would intensify as it moved offshore and out over the warm waters of the Gulf Stream. In fact, R2 dissipated between 2200 and 2239 UTC on 6 March as it moved over the Gulf Stream and approached the strengthening convective Gulf Stream rainband (GSR-3).

Scientists aboard the University of Washington's C-131A research aircraft noted at 2245 UTC that R2 was rapidly dissipating. Photographs taken from the C-131A aircraft at 2134 and 2259 UTC 6 March are shown in Fig. 10. The photograph in Fig. 10a shows a view from the rear of R2 looking northward, parallel to the rainband, when the aircraft was at an altitude of ~ 3.5 km and within the dry, clear slot of low θ_e air. A layer of altostratus and cirrostratus can be seen extending westward from the rear of R2. The base of the altostratus was at ~ 5.0 to 6.0 km. Clearing was evident to the west of R2. A layer of altocumulus can be seen below the dry slot. This picture is consistent with the vertically pointing radar echoes shown in Fig. 7 and discussed in section 5a. The tops of the altocumulus were at ~ 2.5 km.

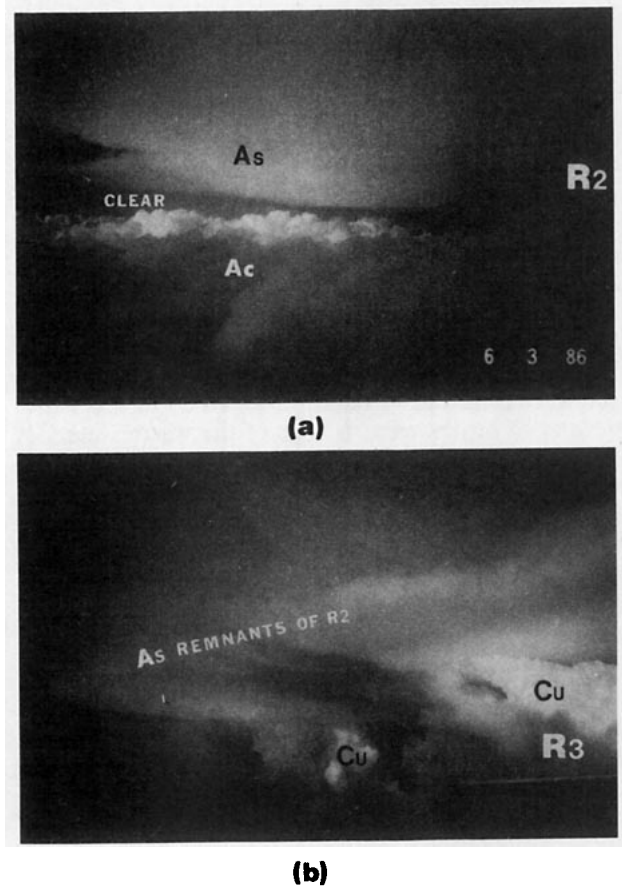

FIG. 10. Aerial photographs (a) looking northward along the rear portion of rainband R2 at 2134 UTC 6 March, and (b) looking northward along the rear of rainband R3 and at the remnants of rainband R2 at 2259 UTC 6 March. In (a) the altostratus cloud is labeled as As and altocumulus as Ac. In (b) the remnants of the rear anvil associated with rainband R2 are labeled as As and the cumulus associated with rainband R3 as Cu.

In contrast, the northward portion of the rear of R3 at 2259 UTC 6 March shows cumulus towers extending into a layer of altostratus. The aircraft flight level at this time was ~4.3 km. The video tape from the nose camera aboard the aircraft reveals that the rear anvil of altostratus, evident in Fig. 10b, was associated with R2 and not the newly developed R3. Cloud tops associated with R3 were estimated to extend to ~7.0 km at 2259 UTC from a comparison of the two photographs shown in Fig. 10, it is clear that the cumulonimbus developed to the rear of the remnants of R2.

The 1800 UTC 6 March 1986 Morehead City CLASS sounding and 0045 UTC 7 March dropwindsonde from the NOAA WP-3D aircraft (launched from 32.9°N, 73.4°W) are shown in Fig. 11. The Morehead City sounding was launched in advance of the upper-level trough, 60 km ahead of the region of maximum radar reflectivity associated with R2 and prior to the development of R3. The 0045 UTC 7 March dropwindsonde was in advance of the upper-level trough and between rainbands GSR-3 and R3. These soundings can be used to examine the stability of the lower troposphere in advance of the upper-level trough over land and over the warm waters of the Gulf Stream.

There was a moistening of the lower troposphere between the time of the Morehead City sounding and the dropwindsonde. The dropwindsonde showed higher temperatures below 800 mb and appreciably more instability than the Morehead City sounding. The dropwindsonde was neutrally stable to near absolutely unstable to dry processes below 840 mb. Lifted indices (LI) were calculated from 1000 to 700 mb for each sounding (Fig. 11). The dropwindsonde had a LI of −4 and the Morehead City sounding was +6. Thus, the dropwindsonde passed through air that was considerably more unstable at lower levels than did the Morehead City sounding. The convective rainband R3 formed in the more unstable region.

The location of the aircraft in relation to the maximum of radar reflectivity associated with R2 was plotted to derive the cross sections in Figs. 8a, 9a and 9b. On the assumption that R2 was relatively two dimensional, the C-131A aircraft at 2155 UTC, in relationship to the maximum of radar reflectivity, should have been well within a region of cloud and precipitation in the vicinity of the main updraft of R2 (according to the vertical air velocity data in Fig. 8b). The video tape from the nose camera aboard the C-131A aircraft, and the PMS 2-D cloud and precipitation data, reveal that at 2155 UTC the aircraft was in clear air at the leading edge of R2. This supports the observation that the width of the core of maximum radar reflectivity associated with R2 was decreasing prior to its dissipation. It also suggests that the main updraft and leading edge of R2 were eroding at 2155 UTC.

As discussed in Part I, R2 was associated with a push of cold dry air aloft, similar to a warm occlusion. The integrity of a warm occlusion, as well as its associated rainbands, depends on the stability of cold, dry air aloft with respect to the underlying air mass. Strong latent and sensible heating of this lower layer erodes this stability. As mentioned in section 5b, R2 was characterized by midlevel convergence associated with the leading edge of cold, dry air aloft. As R2 moved offshore

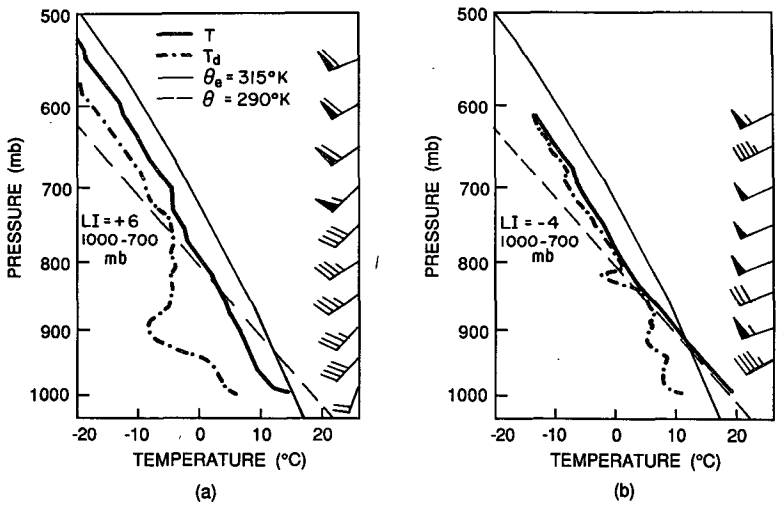

FIG. 11. Soundings (a) from the radiosonde launched at 1800 UTC 6 March 1986 from Morehead City, North Carolina and (b) 0045 UTC 7 March 1986 from a dropwindsonde from the NOAA WP-3D aircraft (located at 32.9°N, 73.4°W). The moist adiabat for a θ_e value of 315 K and dry adiabat of θ equal to 290 K are shown. Temperature (T) and dewpoint temperature (T_d) from the sounding data are indicated by solid and dot dashed lines, respectively. Lifted indices (LI) calculated from 1000 to 700 mb are shown. Winds are shown at an interval of 50 mb and using the same convention as in the legend of Fig. 2.

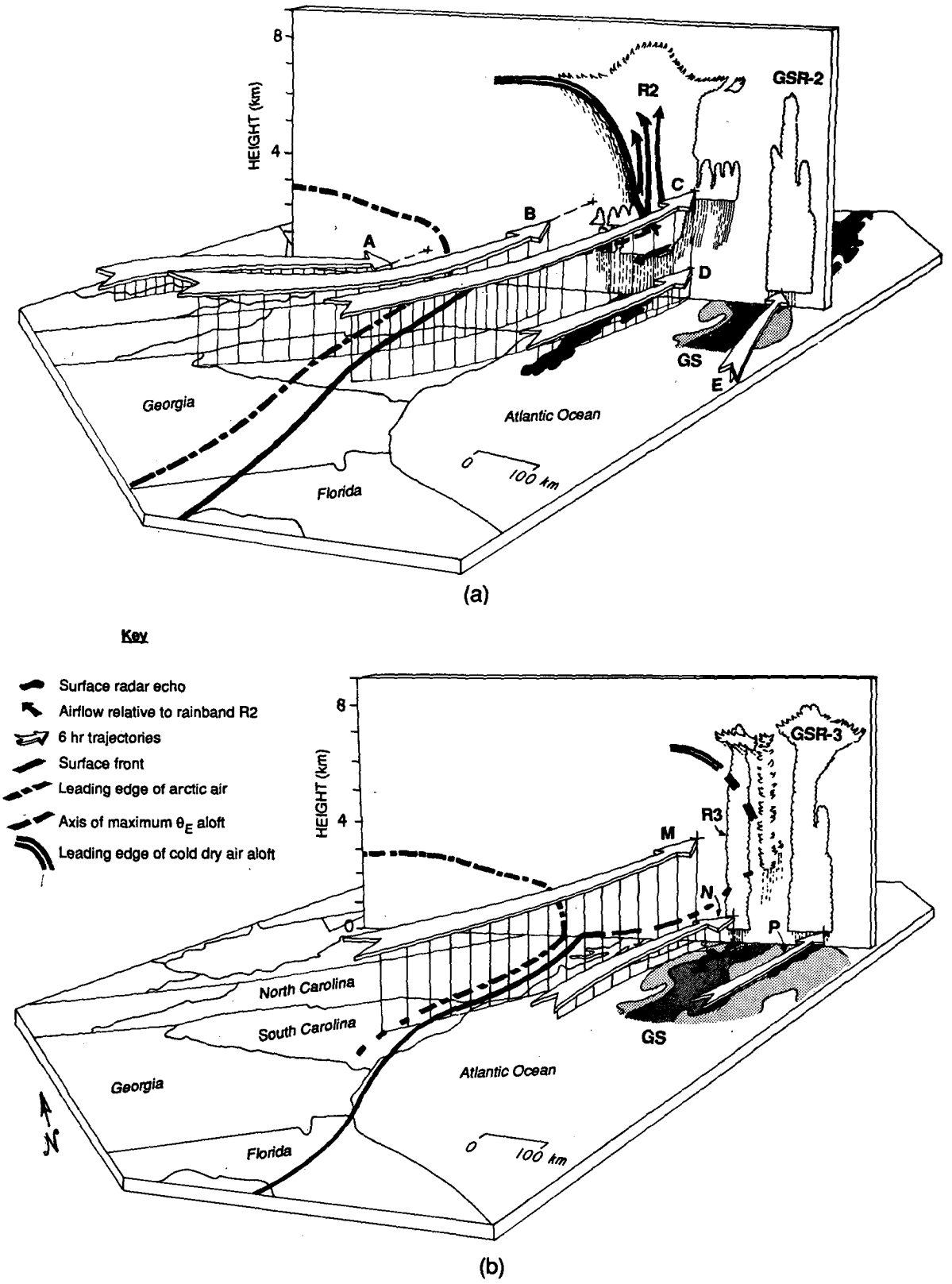

FIG. 12. Schematic depictions in horizontal and vertical planes of the synoptic and mesoscale situations for (a) 1900 UTC 6 March 1986 and (b) 2300 UTC 6 March 1986. Shown are the locations of frontal features, precipitation features, and trajectories of air parcels associated with various portions of the frontal system. The warm-water core of the Gulf Stream (GS) is shown by the dark stippling over the Atlantic Ocean. Sea surface temperatures in this region were ≥24°C, the light stippling indicates sea-surface temperatures between 22°–24°C. Trajectories (broad arrows) shown in (a) are: A—cold air behind the leading edge of arctic air; B—cold, dry air behind the upper-level region of cold-air advection; C—warmer moist air ahead of the zone of cold-

over the warm Gulf Stream, convective instability developed in the region of weakest stability immediately behind R2, where for some time altocumulus had been forming. The subsequent convective mixing destroyed the convergent flow aloft associated with R2. In addition, the compensating downward motion from band GSR-3 may have enhanced the dissipation of R2.

7. Mesoscale synopsis

The essential features of the storm of 6 March 1986 evolved on a synoptic scale as described in Part I. The Rocky Mountains were critical in the establishment of the leeside trough, and in the formation of a warm occluded-type structure; this configuration was responsible for the mesoscale structure of the storm as it passed over North Carolina.

The convergence and lifting of air at the nose of the wedge of cold air aloft produced rainband R2. Thus, the mesoscale airflow and θ_e analysis presented in this paper (see section 5b) is consistent with the larger-scale analysis given in Part I. In turn, the microphysical structure of the storm over the North Carolina coast reflects the mesoscale structure (see section 5a). The release of instability aloft, behind the push of cold air aloft, was also due to the warm occlusion-like frontal structure. In this region, layers of stratocumulus and altocumulus rapidly changed to a band of cumulonimbus as the stability decreased over the Gulf Stream (see section 6d).

The relationship between the warm occlusion-like structure and the mesoscale configuration of this frontal system was strikingly demonstrated by the sudden dissipation of rainband R2. Overland, R2 was maintained by convergence aloft above a stable layer in advance of the push of cold, air aloft (see Figs. 8a and 8b, section 5b). However, when R2 moved over the Gulf Stream strong mesoscale mixing, associated with the Gulf Stream rainband and the convective rainband R3, eroded the stable layer and disrupted the nose of cold, dry air aloft that had been maintained by the synoptic flow, resulting in the dissipation of R2.

The schematics shown in Fig. 12 illustrate both the synoptic and mesoscale configuration of the system as it passed over Cape Hatteras. The air trajectories shown in this diagram, which illustrate the large-scale airflow, were calculated from the NMC nested grid model output. Sea-surface temperatures are from the NOAA-9 satellite for 0747 UTC 7 March 1986.

At 1900 UTC 6 March (Fig. 12a), rainband R2 was situated at the leading edge of the cold-air advection aloft over eastern North Carolina and about 225 km ahead of the surface front. Virga from the altocumulus clouds was ahead of R2. There was a well-defined slot of cool dry air behind the leading edge of cold air, with the virga from altostratus clouds falling into the dry air. Below the dry air, lower-level altocumulus and stratocumulus were present in a region of convective instability. The convective Gulf Stream rainband (GSR-2) was located to the east of the warmest waters of the Gulf Stream.

Trajectory C in Fig. 12a represents the ascending inflow of air into R2 ahead of the push of cold, dry air aloft. Trajectory D is the southwesterly flow of relatively cool dry air that was located beneath the stable layer and in advance of and below R2. The southwesterly flow parallel to the Gulf Stream, and the inflow of air into rainband GSR-2, is shown by trajectory E in Fig. 12a. The descending and then ascending cold, dry air that was observed behind the leading edge of cold-air advection is represented by trajectory B. As discussed in Part I, a shallow region of arctic air was associated with this frontal system; the low-level westerly flow associated with the arctic air is shown by trajectory A.

By 2300 UTC, rainband R2 had dissipated due to a decrease in the low-level stability over the warm waters of the Gulf Stream, the subsequent development of convective band R3 behind R2 and the compensating downdraft of rainband GSR-3. The last precipitation echo associated with rainband R2 detected by the NWS radar at Cape Hatteras was at 2239 UTC 6 March. Thus, the remnants of R2 are represented by the cloud debris in Fig. 12b. The convective rainband R3 developed over the warmer inshore water west of the Gulf Stream and behind the leading edge of cold-air advection aloft and is shown extending through the remnant anvil of altostratus from R2. Gulf Stream rainband GSR-3 developed between 2100 and 2200 UTC (see Fig. 5) and moved eastward. This was the most intense of the three Gulf Stream rainbands.

The low-level flow at 2300 UTC associated with GSR-3 (trajectory P) had a more westerly trajectory across the Gulf Stream than trajectory E, associated with GSR-2, had at 1900 UTC. This increasing westerly component of the low-level flow was most probably responsible for the eastward movement of bands GSR-2 and GSR-3 (see sections 4 and 6b). Trajectory N represents the low-level flow of modified air in advance of and below the push of cold, dry air aloft associated with the development of band R3 and is analogous to trajectory D at 1900 UTC. Trajectory N passed over the warmer inshore waters west of the Gulf Stream while trajectory D remained over the cool inshore waters and the eastern Carolinas. The cool dry air behind the upper-level trough is represented by trajectory M which, like trajectory B in Fig. 12a, originated over the continent.

air advection, associated with rainband R2; **D**—low-level southwesterly flow in advance of and below rainband R2; and **E**—the low-level south-southwesterly flow over the Gulf Stream. Trajectories in (b) are: **M**—cold, dry air behind the upper-level region of cold air advection, analogous to **B** in (a); **N**—low-level southwesterly flow, corresponding to **D** in (a); and **P**—low-level southwesterly flow associated with the Gulf Stream rainband 3.

7. Conclusions

In this paper we have examined the mesoscale precipitation and frontal structure of a mature cyclone of continental origin as it passed over Cape Hatteras, North Carolina, and moved offshore over the warm waters of the Gulf Stream. Our principal conclusions can be summarized as follows.

- The mesoscale structure of the clouds and precipitation over the Carolina coastal plain was a direct consequence of the large-scale synoptic structure. The mesoscale and microphysical analysis presented in this paper are consistent with the synoptic-scale structure presented in Part I.
- The precipitation associated with this system over Cape Hatteras was primarily stratiform in nature and was associated with two rainbands that show strong similarities to the prefrontal surge and wide cold-frontal rainbands observed in occluded cyclones on the Pacific Northwest Coast of the United States.
- The seeder–feeder process probably played an important role in the formation of precipitation in the wide cold-frontal rainband.
- Offshore, in advance of the upper-level trough, precipitation was highly convective in nature, and three rainbands developed over the Gulf Stream. The onset of southwesterly, low-level synoptic flow, with a relatively long fetch over the Gulf Stream, helped to develop the necessary conditions for the development and maintenance of the Gulf Stream rainbands.
- The movement of the Gulf Stream rainbands eastward, and the formation of new Gulf Stream rainbands, was tied to an increasing westerly component of the lower-level winds across the Gulf Stream.
- The general decrease in low-level stability as the push of cold, dry air and associated wide cold-frontal rainband moved over the warm Gulf Stream resulted in the formation of a strong convective rainband just behind the leading edge of cold air aloft. The formation of this rainband, and the compensating downward motions produced by a Gulf Stream rainband, caused the wide cold-frontal rainband to dissipate as it moved over the Gulf Stream.

Finally, by combining information presented in Part I and in this paper, we can obtain some perspective on the time scales of various components (the low-pressure center, the surface frontal features, the pushes of cold air aloft, the cloud bands and rainbands) of this frontal system. The low-pressure center had a lifetime on the order of three days, the surface fronts a lifetime on the order of ~2–3 days, and the two surges of cold air aloft, the prefrontal surge and the primary cold front had lifetimes on the order of days. By contrast, the clouds associated with rainband R1 and the first push of cold air had lifetimes on the order of ~17 hours, and the clouds associated with R2 a lifetime of ~12 hours. Rainbands R1 and R2 had even shorter lifetimes, ~6 and 5 hours, respectively. These observations highlight the variety of phenomena with different lifetimes embedded within frontal systems, and the challenge that this complexity presents to the forecasting of precipitation.

Acknowledgments. Thanks are due to all those who participated in GALE, particularly, Paul Herzegh, for his assistance in the collection of radar data and the flight crew of the C-131A. We also thank Hampton Terry of our group for help in processing the radar data. This research was funded by the Atmospheric Research Section of the NSF, under Grants ATM-8311147 and ATM-8608467.

REFERENCES

Browning, K. A., and G. A. Monk, 1982: A simple model for the synoptic analysis of cold fronts. *Quart. J. Roy. Meteor. Soc.*, **108**, 435–452.

Genesis of Atlantic Lows Experiment (GALE), 1985: Experiment Design, 1985. [Available from the GALE Project Office, National Center for Atmospheric Research, Boulder, Colorado, 80307.]

Fett, R., P. LaViolette, M. Nestor, J. Nickerson and K. Rabe, 1979: Naval Tactical Applications Guide, Vol. 2, Environmental Phenomena and Effects. 161 pp. [Available from the Navy Environmental Prediction Facility, Monterey, CA 93940]

Herzegh, P. H., and P. V. Hobbs, 1980: The mesoscale and microscale structure and organization of clouds and precipitation in midlatitude cyclones. Part II: Warm-frontal clouds. *J. Atmos. Sci.*, **37**, 597–611.

Hobbs, P. V., 1978: Organization and structure of clouds and precipitation on the mesoscale and microscale in cyclonic storms. *Rev. Geophys. Space Phys.*, **16**, 741–755.

——, 1987: The Gulf Stream rainband. *Geophys. Res. Lett.*, **14**, 1142–1145.

——, and J. D. Locatelli, 1978: Rainbands, precipitation cores, and generating cells in a cyclonic storm. *J. Atmos. Sci.*, **35**, 230–241.

——, T. J. Matejka, P. H. Herzegh, J. D. Locatelli and R. A. Houze, Jr., 1980: The mesoscale and microscale structure and organization of clouds and precipitation in midlatitude cyclones. Part I: A case study of a cold front. *J. Atmos. Sci.*, **37**, 568–596.

——, N. T. Funk, R. R. Weiss, Sr., J. D. Locatelli and K. R. Biswas, 1985: Evaluation of a 35 GHz radar for cloud physics research. *J. Atmos. Oceanic Technol.*, **2**, 35–48.

Kreitzberg, C. W., and H. A. Brown, 1970: Mesoscale weather systems within an occlusion. *J. Appl. Meteor.*, **9**, 419–432.

Locatelli, J. D., P. V. Hobbs and K. R. Biswas, 1983: Precipitation from stratocumulus clouds affected by fallstreaks and artificial seeding. *J. Climate Appl. Meteor.*, **22**, 1393–1403.

——, J. M. Sienkiewicz and P. V. Hobbs, 1989: The organization and structure of clouds and precipitation on the mid-Atlantic coast of the United States. Part I: Synoptic evolution of a frontal system from the Rockies to the Atlantic Coast, *J. Atmos. Sci.*, **46**, 1327–1348.

Matejka, T. J., R. A. Houze, Jr., and P. V. Hobbs, 1980: Microphysics and dynamics of clouds associated with rainbands in extratropical cyclones. *Quart. J. Roy. Meteor. Soc.*, **106**, 29–56.

Sethuraman, S., A. J. Riordon, T. Holt, M. Studer and J. Hinman, 1986: Observations of the marine boundary layer thermal structure over the Gulf Stream during a cold air outbreak. *J. Climate Appl. Meteor.*, **25**, 14–21.

Sweet, W., R. Fett, J. Kerling and P. LaViolette, 1981: Air-sea interaction effects in the lower troposphere across the north wall of the Gulf Stream. *Mon. Wea. Rev.*, **109**, 1042–1052.